CHINESE JOURNAL OF PHYSICS VOL. 35, NO. 4 AUGUST 1997

The Science and Technology of Condensed Matter Physics — From Atomic Imaging to Space Research

N.-C. Yeh*
Department of Physics, California Institute of Technology, Pasadena, CA 91125, U.S.A.

(Received May 19, 1997)

Various areas of our ongoing condensed matter physics research which involve both fundamental physics and advanced technology are described. The research topics include studies of the vortex dynamics and pairing symmetry of high-temperature superconductors; development of precision clocks using high-Q superconducting microwave cavities; state-of-the-art measurements of the density and critical phenomena of liquid helium near phase transitions and under microgravity; as well as the physics and device applications of various magnetoresistive perovskites. The experimental scope encompasses techniques from atomic imaging to space research, and the important interplay of fundamental science and frontier technology in our research is also addressed.

PACS. 74.60.-w – Type-II superconductivity.
PACS. 74.50.+r – Proximity effects, weak links, tunneling phenomena, and Josephson effects.
PACS. 75.50.-y – Studies of specific magnetic materials.

I. Introduction

The rapid advances and diversification in condensed matter physics have prompted new development in technology to achieve higher-precision and better-resolution measurements. Conversely, the advances at the technological front have also provided unprecedented opportunities for investigating various fundamental science-related issues in condensed matter physics. In this paper we describe several areas of our ongoing experimental research in condensed matter physics which involve both basic science and advanced technology. The research topics include studies of the vortex dynamics and pairing symmetry high-temperature superconductors; development of precision clocks using high-Q superconducting cavities for both basic research and device applications; state-of-the-art measurements of the density and critical phenomena of quantum fluids near phase transitions; and the physical properties and device applications of magnetoresistive perovskites that exhibit either colossal magnetoresistance or giant ferromagnetic Hall effect. The experimental approach encompasses techniques from atomically-resolved imaging and spectroscopy to microgravity-related space research. The anticipated scientific and technological impact of these studies is also discussed.

II. Superconductivity-vortex dynamics, pairing symmetry, and precision clocks

II-1. Vortex dynamics of high-temperature superconductors

The combined effects of large thermal fluctuations, short coherence lengths, long penetration depths and large mass anisotropies are known to result in novel vortex dynamics in the mixed state of high-temperature superconducting cuprates [I]. A new thermodynamic phase, the vortex-liquid, occurs between a low-temperature vortex-solid phase and the normal state. Despite the rich and novel physics associated with this vortex-liquid state and the phase transitions between the vortex-solid and vortex-liquid [2-8], the thermally-induced vortex motion in the vortex-liquid state results in dissipation which imposes limitation on the usefulness of high-temperature superconductors to lower temperatures. Hence, for practical purposes such as device applications, it is essential to understand how to minimize vortex motion in high-temperature superconductors through the introduction of different types of pinning defects.

We have systematically investigated the effects of static disorder on the vortex dynamics of high-temperature superconductors [6-8]. In the clean limit and for a constant magnetic field, the vortex-solid to liquid transition of $YBa_2Cu_3O_7$ single crystals is consistent with a first-order melting transition [4,7]. On the other hand, in the presence of significant static disorder, the vortex-solid phase becomes glass-like, and the phase transition between the solid and liquid phases becomes second-order [2,3,5]. Depending on the type of static disorder in the superconductors, these second-order vortex phase transitions may be categorized into different universality classes [6-8], as illustrated in Fig. 1. In addition to the variations in the universality classes of phase transitions, correlated static disorder also induces anisotropic vortex dynamics [6-8], as manifested by the changes in the angular dependent vortex phase transition temperatures shown in Fig. 2 for a given magnetic field (H).

In addition to the important effects of symmetry-breaking and anisotropic vortex dynamics induced by static disorder, there are two important consequences associated with the introduction of pinning defects, as illustrated in Fig. 3 and Fig. 4, where the vortex-solid to liquid phase transition temperatures and the critical current densities are shown to be enhanced with the introduction of columnar defects. The physics knowledge derived from these investigations are being applied to improving microwave device performance and manufacturing high-temperature superconducting wires in research laboratories and industry worldwide.

11-2. Studies of the superconducting pairing symmetry using a low temperature scanning tunneling microscope

With the modern invention of low-temperature scanning tunneling microscopy (STM), atomically-resolved images and spectroscopy of materials can be obtained. As exemplified in Fig. 5, our low-temperature scanning tunneling microscope can resolve the atomic structure of a superconducting $NbSe_2$ single crystal to fine details (~ 0.25 Å resolution), including an atomic vacancy on the surface layer. Using this spatially-resolved tool, we have investigated the anisotropic tunneling spectroscopy of a high-temperature superconducting single crystal of $YBa_2Cu_3O_7$ along different k vectors. As illustrated in Figs. 6(a)-(d), the anisotropic superconducting energy gap on a $YBa_2Cu_3O_7$ single crystal along the $\{100\}$, (001) and

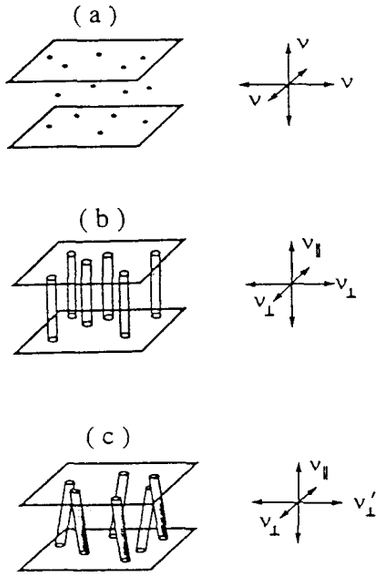

FIG. 1. Effects of static disorder on the vortex phases of high-temperature superconductors [6-8]: **(a)** vortex-glass (VG), (b) Bose-glass (BG), and (c) splayed-glass (SG). Here ν represents the isotropic static exponent of the vortex correlation length in the vortex-glass; $\nu_\parallel$ and $\nu_\perp$ are the parrallel and perpendicular static exponents of the Bose-glass; and $\nu_\perp, \nu_\perp'$ and $\nu_\parallel$ are the anisotropic static exponents of the splayed-glass.

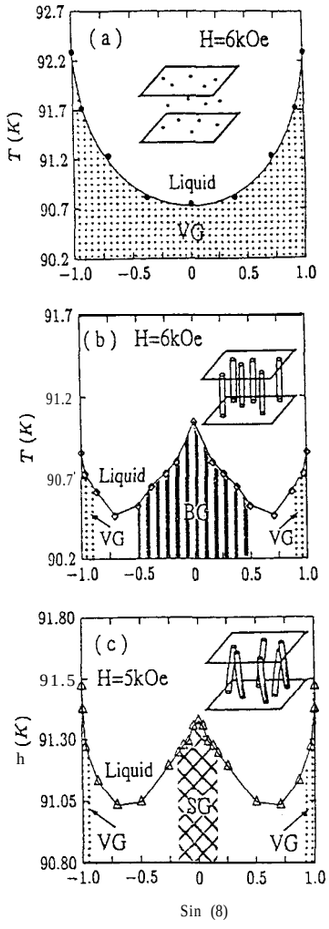

FIG. 2. Representative anisotropic vortex phase diagrams of $YBa_2Cu_3O_7$ single crystals: **(a)** as-grown with dilute twin planes; (b) irradiated with c-axis columnar defects; (c) irradiated with two sets of canted columnar defects at $\pm 7.5°$ relative to the crystalline c-axis. Here θ is the angle between the applied magnetic field H and the crystalline c-axis.

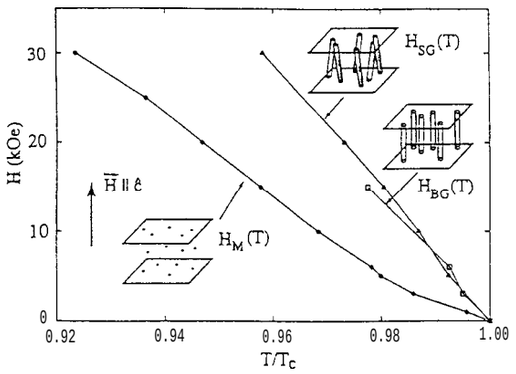

FIG. 3. The magnetic field (H) vs. temperature (T) vortex phase diagram of $YBa_2Cu_3O_7$ single crystals, showing the enhancement of vortex-solid to vortex-liquid transition temperatures with the introduction of columnar defects.

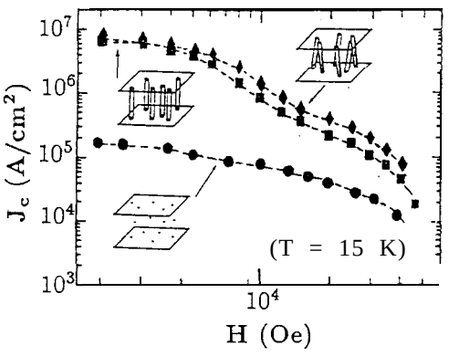

FIG. 4. Enhancement of the critical current densities (J_c) in $Bi_2Sr_2CaCu_2O_x$ due to the presence of columnar defects.

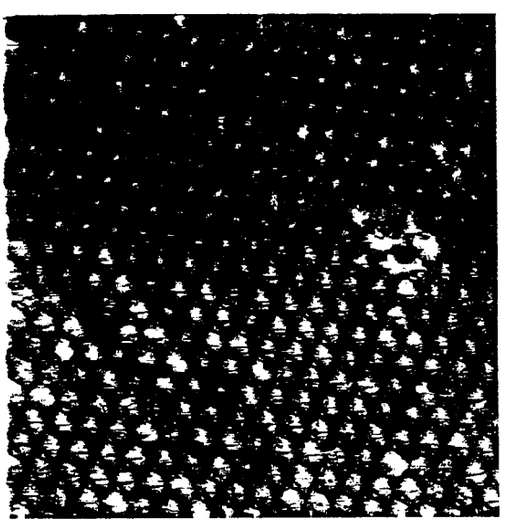

FIG. 5. Surface image of superconducting $NbSe_2$, taken at T = 4.2 K with our low-temperature scanning tunneling microscope. The distance between two consecutive atoms is 3.5 Å.

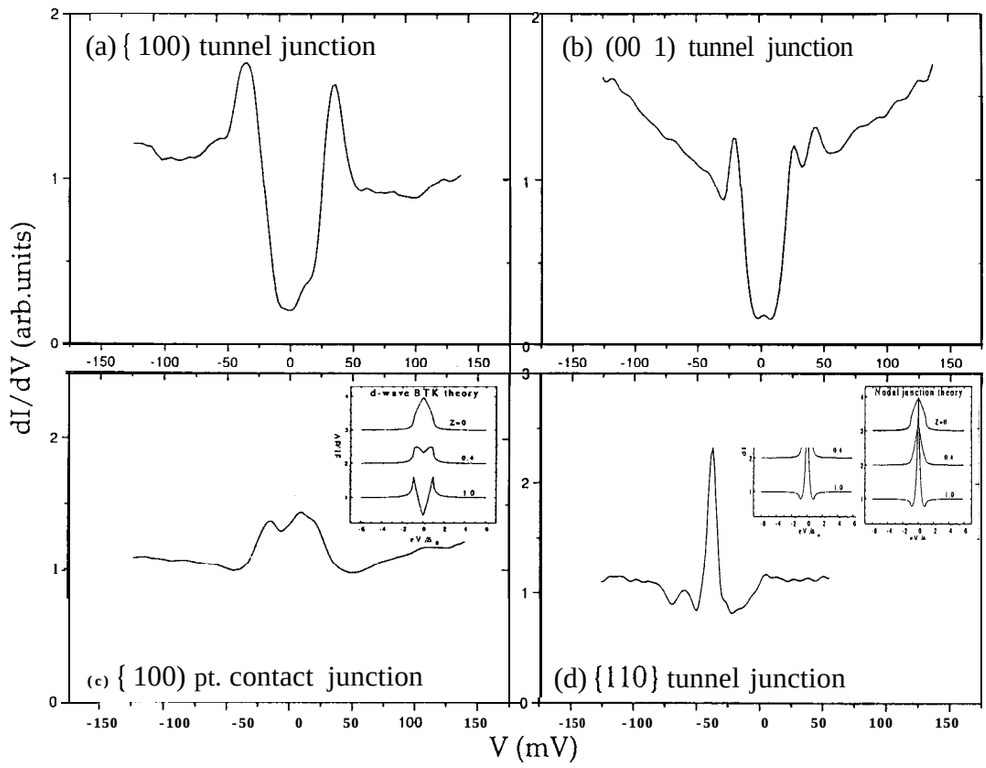

FIG. 6. Differential conductance (dI/dV) between a Pt-tip and a $YBa_2Cu_3O_7$ single crystal at 4.2 K. (See text for detailed descriptions of the spectroscopy.)

{110} directions are obtained by tunneling into these high-symmetry crystalline axes. We find that along the (100) direction the superconducting gap (33 ± 5 meV) is larger than that along the (001) direction (23 ± 5 meV), the latter represents the average gap value in the $k_x k_y$ plane. On the other hand, along the (110) direction, we observe a zero-bias conducting peak [9,10] (Fig. 6(d)) consistent with the prediction of d-wave nodal junction along the (110) direction. We have also observed Andreev reflection spectra along various crystalline axes, as exemplified in Fig. 6(c) for the (100) direction [9]. In the inset of Fig. 6(c), we show the comparison of the theoretical calculations based on the BTK theory [11]:

$$
\begin{aligned}
1 &= \frac{e}{\pi}\int_{-\infty}^{\infty} dE[f(E-eV)-f(E)][1+|A(E)|^2-|B(E)|^2], \\
\mathrm{A} &= \Delta_k^2/[E^2+(\Delta_k^2-E^2)(1\ \mathrm{t}\ 2Z^2)^2], \qquad \mathrm{B} = 1 - \mathrm{A}\ , \qquad (E<\Delta_k), \\
A &= u_k^2 v_k^2/\gamma^2, \qquad B = (u_k^2-v_k^2)^2 Z^2(1\ \mathrm{t}\ Z^2)/\gamma^2, \qquad (E>\Delta_k),
\end{aligned}
\tag{1}
$$

$$\begin{aligned} \gamma^2 &= [u_k^2 + Z^2(u_k^2 - v_k^2)]^2, \quad u_k^2 = 1 - v_k^2 = \frac{1}{2}\left[1 + (E^2 - \Delta_k^2)/E^2\right]^{1/2}, \\ \Delta_k &= \frac{\Delta_0}{2}[\cos k_x - \cos k_y]. \end{aligned} \tag{1}$$

Here V denotes the biased voltage, and f(E) is the Fermi-Dirac function. As shown in Fig. 6(c) and its inset, our Andreev reflection data are consistent with the d-wave BTK theory [11] with a barrier strength parameter $Z = 0.4$. Similarly, we use the d-wave nodal junction model [10] to analyze the (110) conduction peak spectra [9]:

$$\begin{aligned} 1 &= \frac{e}{\pi}\int_{J-\infty}^{\infty} dE[f(E - eV) - f(E)]\left[1 + |a(E)|^2 - |b(E)|^2\right], \\ a &= \frac{1}{D}\left(\frac{v_k}{u_k}\right)\left(\frac{1}{1+Z^2}\right), \quad D = 1 + \left(\frac{Z^2}{1+Z^2}\right)\left(\frac{v_k^2}{u_k^2}\right), \\ b &= \frac{1}{D}\left(\frac{-iZ}{1+iZ}\right)\left[1 + \left(\frac{v_k^2}{u_k^2}\right)\right]. \end{aligned} \tag{2}$$

As shown in Fig. 6(d) and its inset, the d-wave nodal junction model appears to fit our tunneling data (with $Z = 1$) along the (110) direction well. These tunneling spectra unambiguously identify the superconducting pairing symmetry in $YBa_2Cu_3O_7$ as d-wave symmetry. We plan to extend the STM studies to samples with different intrinsic anisotropies, such as the Hg-based HTS compounds of $HgBa_2Ca_{n-1}Cu_nO_{2n+2+\delta}$, $(n = 1, 2, 3)$, in order to unravel one of the most fundamental issues associated with the pairing mechanism of high-temperature superconductors: the effect of interplanar coupling on the superconducting energy gap and its anisotropy.

11-3. High-Q superconducting microwave cavities for precision clocks

Very low-loss superconducting niobium cavities, with the quality factor (Q) as high as $Q \sim 10^{10}$ at $T \leq 2$ K, can be achieved by annealing niobium under ultra-high vacuum ($\sim 10^{-10}$ Torr) and at high temperatures (up to $\sim$ 1800°C). The high-Q superconducting cavities are very stable oscillators which can be used in precision clocks, frequency standards, and various microwave device components. The frequency stability of a superconducting oscillator may be estimated by considering the following equation [12]:

$$\frac{1}{\omega}\frac{\partial \omega}{\partial T} \approx -C_0 \frac{\mu_0 \omega \lambda(0)\, \Delta(0)}{2\Gamma \quad k_B T^2} \exp\left[-\frac{\Delta(0)}{k_B T}\right], \tag{3}$$

where ω denotes the angular frequency of a resonant mode in a superconducting cavity with a geometric factor Γ, C_0 is a constant of the order of unity, X(0) is the zero temperature penetration depth, μ_0 is the vacuum permeability, k_B is the Boltzmann constant, and A(0) is the zero-temperature superconducting energy gap. Using the material parameters for Nb, and assuming that w $= 2\pi$ x 10^{10}sec^{-1}, we find that $(\partial\omega/\partial T)/\omega \approx -10^{-8}$K^{-1}. Incorporating modern high-resolution thermometry (HRT) based on the SQUID (Superconducting Quantum Interference Device) technology, the temperature of the superconducting cavity can be controlled to a stability of AT $<\sim 10^{-10}$ K. Hence, the corresponding frequency

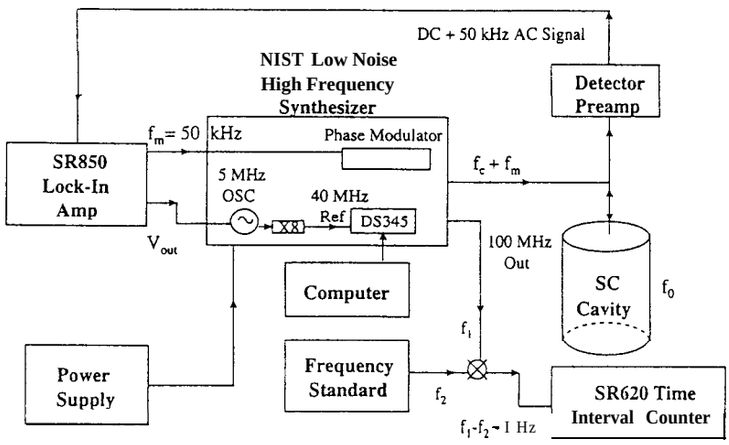

FIG. 7. Block diagram of the phase-locked loop for our precision density measurements of liquid helium using a superconducting (SC) niobium microwave cavity. The principle of operation is to compare the resonant frequency of the superconducting cavity, f_0, with that generated by the low-noise high-frequency synthesizer, f_c, so that the feedback voltage (V_{out}) is proportional to the frequency difference $(f_c - f_0)$, and the resonant frequency f_0 can be read to high precisions by the comparison of $(f_c - f_0)$ with a quartz frequency standard.

stability $(\Delta\omega/\omega)$ of a high-Q superconducting niobium cavity can be as good as one part in 10^{18}. This capability may be achieved by using the state-of-the-art frequency control and readout system, the phase-locked loop, as schematically illustrated in Fig. 7. With the phase-locked loop and a niobium microwave cavity of Q = $10^9 \sim 10^{10}$, we expect to achieve superconducting oscillators with a frequency stability of one part in $10^{17} \sim 10^{18}$.

The high-resolution oscillators based on superconducting cavities can further achieve high accuracy in the frequency when compared with accurate atomic clocks. We are in the process of constructing and optimizing the superconducting cavity-based oscillators, in order to achieve state-of-the-art precision clocks for applications ranging from gravitational wave detection to space navigation.

III. Critical phenomena of superfluidity under gravity and microgravity

As mentioned in the previous section, modern microwave technology combined with high-Q resonators can achieve frequency readout and control with a resolution up to one part in $10^{17} \sim 10^{18}$. Such high-resolution measurements are better than most experimental techniques, and therefore may be applied to research areas that require state-of-the-art precisions. We have recently initiated a research project which aims at unravelling the fundamental nature of continuous phase transitions by studying the static and dynamic critical properties of condensed phases of helium near phase transitions with the use of various state-of-the-art technologies that can provide unprecedented precisions. The basic

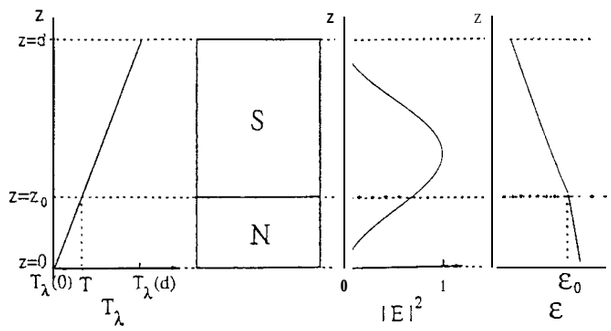

FIG. 8. A schematic showing how the gravity-induced density profile of helium in the superconducting microwave cavity can be deconvolved by the electric field of the TE_{011} mode. Here z_0 denotes the superfluid (S) - normal (N) fluid interface position, and d is the height, of the cavity. The lambda transition temperatures are $T_\lambda(0)$ for the bottom of the cavity and $T_\lambda(d)$ for the top of the cavity.

concept is to utilize the unique capability of resolving the resonant frequencies of a helium-filled superconducting microwave cavity to extremely high precision (better than one part in 10^{17}), in conjunction with the high-resolution thermometry (HRT) and high-resolution pressure control, to obtain precise measurements of the density and the phase transition temperatures of helium. The principle of using microwave techniques to perform precision density measurements of the helium in condensed phases is based on the Clausius-Masotti relation which relates the density (p) of liquid ^{4}He to its dielectric constant ε:

$$\frac{\varepsilon - 1}{\varepsilon + 2} = \frac{4\pi\rho\alpha_p}{3M}, \tag{4}$$

where α_p is the polarizability and M the molecular weight of helium. If we contain helium in a high-Q superconducting microwave cavity, the temperature-dependent dielectric constant of helium will couple to the electric field of the resonant modes in the cavity, yielding temperature-dependent frequency shifts (Δf) relative to the resonant frequency (f_0) at $T = T_\lambda$ according to the following relation:

$$\frac{\Delta f}{f_0} = \frac{\int_{V_0}(\Delta\varepsilon|E_0|^2)dV}{\int_{V_0}(\varepsilon|E_0|^2)dV}, \tag{5}$$

where $\Delta\varepsilon$ is the temperature-dependent change in dielectric constant relative to the dielectric constant at T_λ, E_0 is the electric field of the resonant mode in the cavity, and V_0 is the volume of the microwave cavity. Thus, the density ρ can be obtained from Eqs. (4) and (5). As illustrated in Fig. 8 and in Ref. [13], even under the influence of gravity which gives rise to a gradient in the superfluid Lambda transition $T_\lambda(z)$, with z being the position measured from the bottom of the microwave cavity, our numerical simulations have demonstrated that our microwave techniques together with the fine resolution in detecting the

temperature-dependent frequency shifts $(\Delta f/f_0)$ can be transformed into high resolutions in the dielectric constant $(\Delta\varepsilon/\varepsilon)$ as well as the density, thereby identifying the Lambda transition temperature for a given pressure to a very high precision. The resolution can be further improved by at least two orders of magnitude under the microgravity environment.

Our current capability can resolve frequencies to better than one part in 10^{17}, which transforms into resolving the density to one part in 10^{14} under microgravity if not limited by the current HRT capability. (Current HRT capability for temperature control at $\sim 10^{-11}$ K would yield a density resolution to one part in 10^{12}, about more than four orders of magnitude better than other measurement techniques achievable to date). Hence, in principle both the phase transition temperatures and density-related critical properties of helium, such as the static and dynamic critical exponents and the amplitude coefficients associated with the thermal expansion coefficient β_P[14] can be determined to unprecedented precisions using the high-Q microwave techniques.

IV. Physics and applications of magnetoresistive perovskites

IV-l. The physical origin of colossal magnetoresistance in $Ln_{1-x}M_xMnO_3$ and potential device applications

Recent discovery of the colossal negative magnetoresistance (CMR) in the perovskite manganites [15-17], $Ln_{1-x}M_xMnO_3$ (Ln: trivalent rare earth ions, M: divalent alkaline earth ions) has spurred intense research in understanding the origin and providing further improvement of the magnetoresistive effects. Our recent experimental studies [18-22] have unambiguously identified two important criteria for the occurrence of CMR in the manganites. One is the double-exchange interaction [23,24], the other is the lattice distortion associated with both the Jahn-Teller effect [16] and the ionic size mismatch between the Mn ions and La (Ca) ions [25]. These two criteria result in half-metallic ferromagnetism below the Curie temperature (T_C)[25]. As illustrated in Fig. 9, the large exchange energy split between the majority and minority bands results in complete spin polarization in the ferromagnetic state, in contrast to typical ferromagnetic metals (such as Ni) where the energy splitting between the majority and minority carriers below T_C is much smaller than the conduction bandwidth, yielding a small fraction of spin polarization [17]. The half-metallicity has an important consequence on the electrical conduction [17,20,22,25]. In the presence of magnetic domains below T_C, any misalignment of the spins between two adjacent domains will result in a large energy barrier for the conducting carriers and therefore a large resistivity in the absence of an external magnetic field. The application of a magnetic field aligns the spins in different magnetic domains, thereby lowering the energy barrier for carriers and yielding colossal negative magnetoresistance.

The complete spin polarization due to the half-metallic ferromagnetism in the manganites has a great promise for device applications. For instance, we may consider injecting spins from the manganites into a high-temperature superconductor via epitaxial thin film growth of $Ln_{1-x}M_xMnO_3$ on top of a high-temperature superconductor (e.g., $YBa_2Cu_3O_7$) film. By injecting a current through the manganites, polarized carriers will diffuse into the superconductor underneath, resulting in Cooper-pair breaking and the suppression of superconductivity. Therefore the superconducting critical current may be varied by controlling the magnitude of the magnetic current. This concept can be used to develop three-terminal

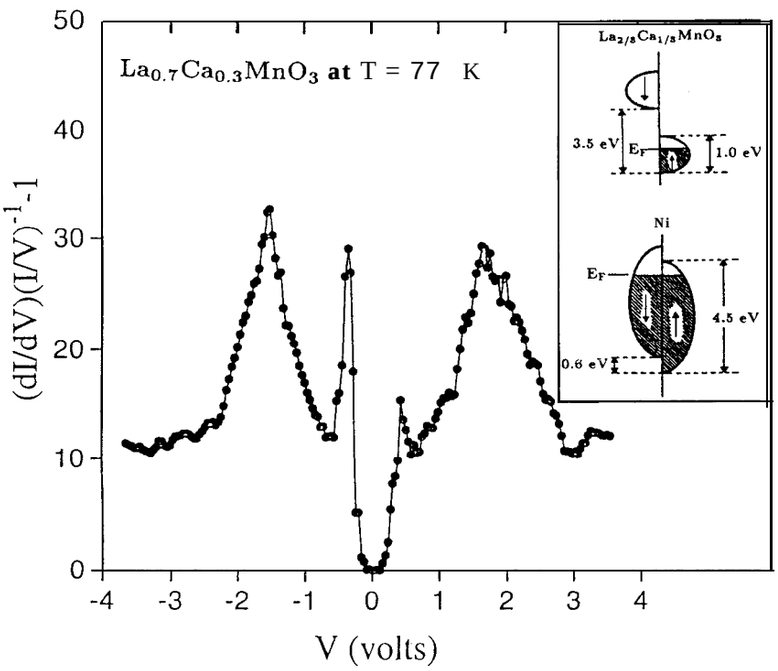

FIG. STM spectroscopy data for an $La_{0.7}Ca_{0.3}MnO_3$ epitaxial film on $LaAlO_3$ taken in the ferromagnetic state at 77 K ($\ll T_C \approx 260$ K), plotted as the normalized conductance vs. the sample bias voltage (V). The pronounced peaks at ± 1.75 eV and a gap structure with edges at ± 0.5 eV. The spectroscopy is in excellent agreement with the density of states calculated by Pickett and Sighn [25] for the exchange energy splitting of the majority and minority bands. The inset is a schematic comparison between a half-metallic ferromagnet such as $La_{0.7}Ca_{0.3}MnO_3$ and a typical metallic ferromagnet Ni. Note that the latter yields a small fraction of spin polarization, in contrast to the complete spin polarization in the manganites.

devices for a wide range of applications, and is another example of advancing technology from new understanding of fundamental physics.

IV-2. Giant ferromagnetic Hall resistivity in $Ln_{1-x}M_xCoO_3$ **and potential device applications**

The cobaltites $Ln_{1-x}M_xCoO_3$ are interesting magnetic materials particularly because of the coexistence of multiple spin configurations in the Co ions [26]. For $x = 0.15 \sim 0.6$, these cobaltites are ferromagnetic at low temperatures. It is known that clusters of high-spin Co ions form better conducting regions which are imbedded in the less conducting matrix consisting of low-spin Co ions [26]. We have recently discovered giant ferromagnetic Hall effects in $La_{1-x}Ca_xCoO_3$ epitaxial films with $x = 0.2$, 0.3, 0.5 and at $T < T_C$ [21].

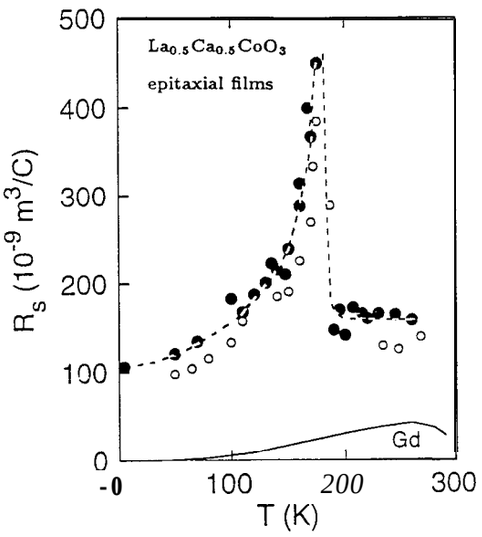

FIG. 10. The ferromagnetic Hall coefficient R_s vs. temperature T data of an $La_{0.5}Ca_{0.5}CoO_3$ epitaxial film on $LaAlO_3$, compared with the corresponding data of Gd. The maximum in R_s occurs near T_C in both samples, and the magnitude of R_s in $La_{0.5}Ca_{0.5}CoO_3$ is significantly larger than that in Gd.

For all Ca-doping levels, the ferromagnetic Hall resistivity (ρ_{xy}) is found to be larger than any known single-phase ferromagnets, as exemplified in Fig. 10 where the ferromagnetic Hall coefficients R_s *as a* fucntion of the temperature for $La_{0.5}Ca_{0.5}CoO_3$ and Gd are compared. Here R_s is related to the Hall resistivity by the following expression:

$$\rho_{xy} = R_H B + R_s \mu_0 M, \tag{6}$$

where R_H is the normal Hall coefficient due to the Lorentz force on carriers, B is the magnetic induction, and M is the magnetization. Another interesting finding is that the Hall resistivity increases significantly as the Ca doping level decreases, and the cobaltites approaches the magnetic percolation threshold [21]. Although to date there is lack of quantitative theoretical understanding of the giant ferromagnetic Hall effect [21], our studies have revealed two important criteria that are closely associated with the enhancement of the ferromagnetic Hall effect. One is the large spin fluctuations amongst the multiple spin configurations near T_C, the other is the presence of magnetic percolating process.

The giant ferromagnetic Hall effect in the cobaltites may be used as sensitive magnetometers which operate at temperatures significantly higher than liquid helium temperatures. As shown in Fig. 11, the ρ_{xy}-vs.-H data for a thin film of $La_{0.7}Ca_{0.3}CoO_3$ shows an extremely steep slope near $T_C(\approx 180\text{K})$. This sensitive change with magnetic fields near $H=0$ may be considered for making low-field magnetometers. The device specifications based on these cobaltites may be particularly useful for lower-cost magnetometers in unmanned space missions, such as for magnetic field detections on the surface of Mars.

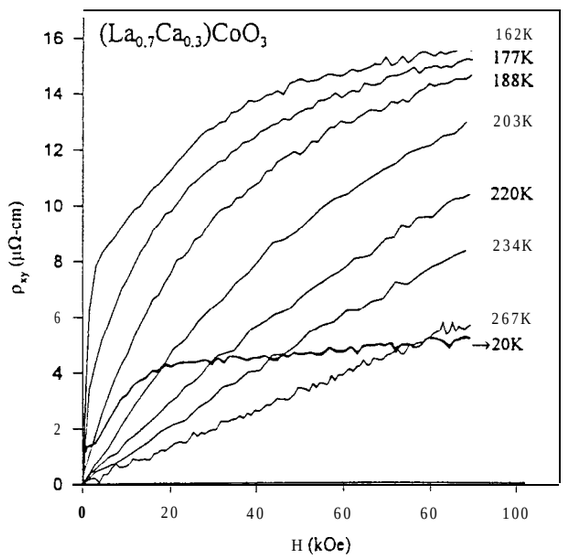

FIG. 11. The Hall resistivity (ρ_{xy}) vs. magnetic field (H) isotherms of a $La_{0.7}Ca_{0.3}CoO_3$ epitaxial film on $LaAlO_3$ substrate. The Curie temperature T_C is approximately 180 K.

V. Summary

We have described some of our current research efforts in condensed matter physics. The research topics include vortex dynamics and pairing symmetry of high-temperature superconductors; development of precision clocks for gravitational physics studies and space navigation; state-of-the-art measurements of the density and critical phenomena of helium near phase transitions under microgravity, using high-Q superconducting microwave cavities; and the physics and device concepts of magnetic perovskites with either colossal magnetoresistance or giant ferromagnetic Hall resistivity. These examples clearly underscore the mutual enhancement of fundamental science and frontier technology in modern condensed matter physics research.

Acknowledgment

The research at Caltech is supported by the National Aeronautics and Space Administration (NASA), National Science Foundation (NSF), Office of Naval Research (ONR), and the Packard Foundation. Part of the research was performed by the Center for Space Microelectronics Technology, Jet Propulsion Laboratory, Caltech, under a contract with NASA. The heavy-ion irradiation was performed at GRANIL in Cean, France.

References

* In collaboration with J. Y. T. Wei, A. V. Samoilov, C.-C. Fu, G. Beach, and J. Huyhn at Caltech; W. Jiang, R. P. Vasquez, D. M. Strayer at the Jet Propulsion Laboratory ; M. Konczykowski at the Ecole Polytechnique in France; F. Holtzberg at IBM, Thomas J. Watson Research Center; and M. Strasik at the Boeing Defence & Space Group.

[1] For a general theoretical review of the vortex dynamics of high-temperature superconductors, see G. Blatter et al., Rev. Mod. Phys. 66, 1125 (1994).
[2] D. S. Fisher, M. P. A. Fisher, D. A. Huse, Phys. Rev. B43, 130 (1991).
[3] D. R. Nelson and V. M. Vinokur, Phys. Rev. Lett. 68, 2398 (1992); Phys. Rev. B48 13060 (1993).
[4] R. E. Hetzel, A. Sudbφ and D. A. Huse, Phys. Rev. Lett. 69, 518 (1992).
[5] T. Hwa, D. R. Nelson, and V. M. Vinokur, Phys. Rev. B48 1167 (1993).
[6] N.-C. Yeh et al., Physica A200, 374 (1993); *Advances* in Superconductivity *-VII* (Springer-Verlag, Tokyo, 1994); Ferroelectrics 177, 143 (1996).
[7] W. Jiang et al., Phys. Rev. Lett. 74, 1438 (1995); to appear in J. Phys.: Condens. Matter, *(1997).*
[8] D. S. Reed *et al.*, Phys. Rev. **B51**, 16448 (1995); Phys. Rev. B49, 4384 (1994); Int. J. Mod, Phys. **B10**, 2723 (1996).
[9] J. Y. T. Wei, N.-C. Yeh, and M. Strasik, submitted to Phys. Rev. Lett. (1997).
[10] C. R. Hu, Phys. Rev. Lett. 72, 1562 (1994); J. H. Xu, J. H. Miller, and C. S. Ting, Phys. Rev. B53, 3604 (1996).
[11] G. E. Blonder, M. Tinkham, and T. M. Klpawijk, Phys. Rev. B25, 4515 (1982).
[12] V. B. Braginsky, V. P. Mitrofano and V. I. Panov, *Systems with Small Dissipation* (The University of Chicago Press, 1985).
[13] N.-C. Yeh, W. Jiang, D. M. Strayer, and N. N. Asplund, Czech J. Phys. 46 Suppl. **S3**, 181 (1996).
[14] G. Ahlers, Rev. Mod. Phys. 52, 489 (1980).
[15] R. von Helmolt *et al.*, Phys. Rev. Lett. 71, 2331 (1993); S. Jin *et al.*, Science 264, 413 (1994); Appl. Phys. Lett. 66, 382 (1995); Appl. Phys. Lett. 67, 557 (1995).
[16] A. J. Millis, P. B. Littlewood, and B. I. Shraiman, Phys. Rev. Lett. 74, 5144 (1995); A. J. Millis, B. I. Shraiman, R. Mueller, Phys. Rev. Lett. 77, 175 (1996).
[17] H. Y. Hwang *et al.*, Phys. Rev. Lett. 77, 2041 (1996).
[18] N.-C. Yeh, R. P. Vasquez, D. A. Beam, C.-C. Fu, J. Huynh, and G. Beach, J. Phys.: Condens. Matter 9, 3713 (1997); N.-C. Yeh, R. P. Vasquez, C.-C. Fu, J. Y. T. Wei, J. Huynh, G. Beach, and D. A. Beam, J. Appl. Phys. 81, 5499 (1997).
[19] A. V. Boris, A. V. Bazhenov, N. N. Kovaleva, A. V. Samoilov, N.-C. Yeh, and R. P. Vasquez, J. Appl. Phys. 81, 5756 (1997).
[20] N.-C. Yeh *et al., Epitaxial Oxide Thin Films -III* (Mater. Res. Soc. Proc., San Francisco, 1997).
[21] A. V. Samoilov, G. Beach, and C.-C. Fu, N.-C. Yeh, R. P. Vasquez, submitted to Phys. Rev. Lett. (1997); A. V. Samoilov, N.-C. Yeh and R. P. Vasquez, *Epitaxial Oxide Thzn Films - III* (Mater. Res. Soc. Proc., San Francisco, 1997).
[22] J. Y. T. Wei, N.-C. Yeh, and R. P. Vasquez, submitted to Phys. Rev. Lett. (1997).
[23] G. H. Jonker and J. H. van Santen, Physica 16, 337 (1950); J. H. van Santen and G. H. Jonker, Physica 16, 599 (1950); C. Zener, Phys. Rev. 82, 403 (1951).
[24] E. 0. Wollan and W. C. Koehler, Phys. Rev. 100, *545 (1955).*
[25] W. E. Pickett and D. J. Singh, Phys. Rev. **B53**, 1146 (1996).
[26] J. B. Goodenough, A. Wold, R. J. Arnott, and N. Menyuk, Phys. Rev. 124, 373 (1961); J. B. Goodenough, in Progress *in Solid State Chemistry,* Vol. 5, ed. H. Reiss (Pergamon Press, 1971).